Contents lists available at ScienceDirect

Journal of Wind Engineering & Industrial Aerodynamics

The influence of terrain on the mean wind flow characteristics in a fjord

Etienne Cheynet [a,b,*], Shengnan Liu [b], Muk Chen Ong [b], Jasna Bogunović Jakobsen [b],
Jónas Snæbjörnsson [b,c], Inno Gatin [d]

[a] Geophysical Institute and Bergen Offshore Wind Centre, University of Bergen, 5007, Bergen, Norway
[b] Department of Mechanical and Structural Engineering and Materials Science, University of Stavanger, N-4036, Stavanger, Norway
[c] Department of Engineering, Reykjavík University, Reykjavík, Iceland
[d] Department of Energy, Power Engineering and Environment, University of Zagreb, Ivana Lučića 5, 10000, Zagreb, Croatia

ABSTRACT

Flow conditions in complex terrains such as fjords are highly three-dimensional and thus not properly captured by the wind flow models developed for homogenous terrains. In the present study, we explore the potential of computational fluid dynamics (CFD) simulations relying on the steady 3D Reynolds-averaged Navier-Stokes equations to complement in-situ measurements from a long-span bridge in a narrow fjord. The validation is done using velocity data recorded in 2017 and 2018 by nine sonic anemometers mounted above the deck of a fjord-crossing suspension bridge. The flow characteristics studied are the along-bridge profile of the mean wind velocity, mean wind direction and mean angle of attack. The simulated flow shows that the non-uniform distributions of the mean angles of attack and wind direction along the bridge span are likely due to side-valley flows, which under certain conditions, predominate over those coming from the main valley. The measurements suggest that wind conditions corresponding to the dominating side-valley flows are associated with a high turbulence intensity at the bridge deck position. The paper highlights the complementary role of CFD studies and in-situ measurements for the design of a wind-sensitive structure, which may not be available using traditional semi-empirical modelling of topography effects.

1. Introduction

In the initial design of long-span bridges, the natural wind is commonly modelled with a zero-mean angle of attack (AOA) and uniform mean wind speed in the horizontal plane. In a canyon or mountainous valley, these assumptions may no longer be valid, which could significantly affect the design of long-span bridges. This calls, therefore, for a more in-depth investigation of the mean flow characteristics in complex terrains.

Among the family of "complex terrains", which is a generic term employed in the literature to describe any irregular relief, the case of a narrow fjord may correspond to one of the highest levels of complexity. A fjord is defined as a u-shaped valley, the floor of which is covered by the sea and entrenched between steep hills and high mountains with slopes that can be greater than 45°. In the following, the term "narrow fjord" refers to the case of a fjord with a width below 2 km.

To study wind conditions in such environments, the traditional approach relies on field measurements complemented by wind tunnel

tests (McAuliffe and Larose, 2012; Lystad et al., 2018; Flay et al., 2019). Wind tunnel tests are a time-saving approach, motivated by the fact that traditional point-measurement devices, such as anemometers, cannot easily be deployed in a fjord before bridge construction. Anemometers have limited capabilities in describing the spatial variability of the flow and years of monitoring may be required to cover the wind conditions of interest. Remote sensing of wind with, e.g. scanning Doppler wind lidar technology, extends the size of the spatial domain in which the mean flow is recorded (Cheynet et al., 2017b, 2016b). However, the maximum scanning range of the lidars may not be sufficient to cover the full area of interest, especially in wide fjords. The flow conditions in heterogeneous terrains have been studied in wind tunnels since the 1980s (Meroney, 1980; Cermak, 1984). Some recent wind tunnel tests, motivated by the potential of wind energy in mountainous areas (McAuliffe and Larose, 2012; Mattuella et al., 2016), or by the need to cross valleys with bridges (Hu et al., 2015; Li et al., 2017; Song et al., 2020; Tang et al., 2020) have shown promising potential in studying local topographic effects. However, scaling down topographic effects raises major challenges (Bowen,

---

2003).

To describe the wind conditions in complex terrain at a microscale level, numerical models can also be used to complement wind tunnel tests. The term "microscale" refers here to a spatial dimension of few meters up to approximatively 1 km and encompasses most of the length scales of turbulence (Fortak, 1982). For industrial and design applications, it is fundamental that the computational cost remains as low as possible. This requirement can be fulfilled by focusing on the mean flow characteristics as a first indicator of the influence of the local terrain on the wind conditions.

To explore numerically the flow conditions in complex terrains, mass-consistent codes (Sherman, 1978; Ratto et al., 1994; Burlando et al., 2007b) have been developed since the 1970s. Such models rely on in-situ measurements to set the initial conditions. Therefore, the performances of mass-consistent models are highly dependent on the positions of the sensors (Zhang, 2015). This implies also that mass-consistent codes may underperform in a narrow fjord due to the restricted range of sensor locations. Besides, such codes generally use a terrain-following coordinate system, which is known to lead to non-negligible numerical errors when the terrain slopes become higher than 30° (Mahrer, 1984), which are commonly found in fjords or gorges.

An increasing spatial resolution implies a more realistic representation of the terrain slopes. Therefore, wind flow modelling using a terrain-following coordinate system is limited by the spatial resolution of the digital terrain models. For example, using a terrain-following coordinate system, state-of-the-art atmospheric modelling systems such as the Weather Research and Forecasting (WRF) model (Shamarock et al., 2008; Powers et al., 2017) cannot be easily applied with horizontal resolutions finer than several hundreds of meters. Nevertheless, it should be noted that the current development of the Immersed Boundary Method within the WRF code (Lundquist et al., 2010, 2012) is promising for large-eddy simulation (LES), as shown by the high-resolution, non-idealized, steep complex terrains study by Arthur et al. (2018). However, the computational cost of LES is a major shortcoming for industrial applications.

High-resolution microscale computational fluid dynamic (CFD) simulations relying on the steady Reynolds-averaged Navier-Stokes (RANS) method are attractive as they are not as computationally intensive as LES-based approaches. The complex boundary conditions of such microscale models can be established using mesoscale atmospheric models such as WRF simulations. Such a coupling has become increasingly popular in the field of wind resource assessment or urban dispersion modelling (Baik et al., 2009; Rodrigues et al., 2016; Bilal et al., 2016; Temel et al., 2018; Barcons et al., 2018). However, in complex terrain, coupling mesoscale and microscale models is a challenging task. It requires a network of in-situ measurements at strategic locations, for example, the bottom of valleys. The deployment of a network of wind sensors is rarely possible in a fjord because of the predominance of areas with deep-water or high mountains. Therefore, setting the boundary conditions of the computational domain using a mesoscale model is out of the scope of the present study. This implies also that the present study focuses exclusively on micro-scale flow simulation.

In the case of the steady RANS method, the focus is generally on the mean flow characteristics. Among them, the mean wind speed, the yaw angle β and the incidence angle α are fundamental parameters to estimate the wind load on a bridge deck. The yaw angle is defined here as the angle between the wind direction and a horizontal line perpendicular to the span axis. The knowledge of both β and α is required to compute the cross-sectional drag force F_D, lift force F_L and overturning moment F_M:

$$\begin{bmatrix} F_D \\ F_L \\ F_M \end{bmatrix} = \frac{1}{2}\rho B U_{\text{rel}}^2 \begin{bmatrix} C_D(\alpha, \beta) \\ C_L(\alpha, \beta) \\ C_M(\alpha, \beta) \end{bmatrix} \tag{1}$$

where B is the deck width; U_{rel} is the relative wind speed expressed in the bridge-based coordinate system, based on the wind velocity components in the wind-based coordinate system as well as α and β (Fig. 1); $C_D(\alpha, \beta)$, $C_L(\alpha, \beta)$ and $C_M(\alpha, \beta)$ are the aerodynamic drag, lift and overturning moment coefficients which depend on both α and β (Zhu et al., 2002). The forces, which refer to the wind coordinate system are, for structural analysis, transformed into loads in the bridge-based coordinate system. More details on the expression of the aerodynamic wind load on a bridge deck under arbitrary incidence and yaw angles can be found in e.g. Strømmen and Hjorth-Hansen (1995); Zhu and Xu (2005).

As stated by Blocken et al. (2015), CFD modelling of microscale flow in complex terrains validated by field measurements is a topic that has been little studied apart from the case of isolated hills. This topic was only shortly covered in the reviews by Murakami (1997) or Blocken (2014), reinforcing the idea that CFD microscale flow in complex terrain is an emerging issue in civil engineering. Although this topic has been addressed since the 2000s in the field of wind energy (Dhunny et al., 2017; Rodrigues et al., 2016; Toja-Silva et al., 2018) and aviation safety (Eidsvik et al., 2004; Rasheed and Sørli, 2013), wind engineering applications have a different focus in terms of flow characteristics, requiring a different approach. For long-span bridge design, which is the topic discussed hereafter, CFD studies of the flow field in mountainous terrain were recently conducted in China (Hu et al., 2018; Tang et al., 2020) but this topic remains largely unexplored in fjord-like topographies.

Table 1 shows that previous microscale flow simulations in complex terrain using the steady RANS method rely on digital elevation models (DEM) with diverse levels of accuracy. A horizontal spatial resolution finer than 90 m is likely required to model properly the local topography effects, such as flow separation around hills (Temel et al., 2018; Rasheed and Sørli, 2013). A spatial resolution around or finer than 30 m might be required for a narrow fjord. Besides, the accuracy of the DEM depends heavily on the sensors used and, therefore, the data source (Table 1). For example, the DEMs produced by the Shuttle Radar Topography Mission (SRTM) (Van Zyl, 2001; Farr et al., 2007) are freely available since 2015 with a horizontal spatial resolution of ca. 30 m. The Advanced Space-borne Thermal Emission and Reflection Radiometer (ASTER) sensor is also used to generate DEM with a spatial resolution of 30 m since 2011 (Tachikawa et al., 2011). However, in highly complex terrain, the ASTER 30-m may be substantially less accurate than the SRTM 30-m dataset (Kervyn et al., 2008), which was also observed in the case of the Lysefjord.

Knowledge of the mean flow characteristics provides already valuable information that can be exploited to better model turbulence effects on
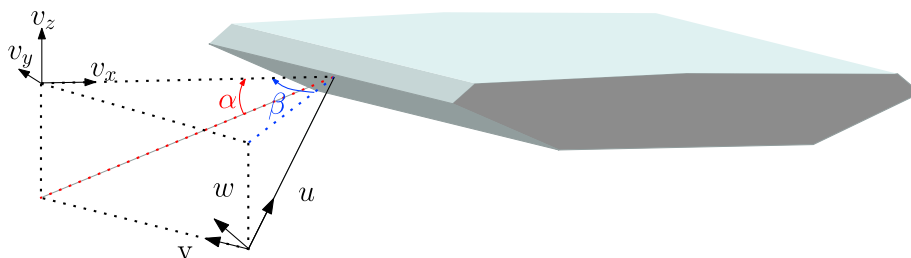

Fig. 1. Schematic of the wind field $\{u, \ v, \ w\}$ in a wind-based coordinate system and its projection on the bridge-based coordinate system $\{v_x, \ v_y, \ v_z\}$, using the yaw angle β and the incidence angle α.

Table 1

Microscale CFD simulations of mean wind velocity in complex terrain with the steady RANS method. The term "not provided" indicates that the information conveyed is incomplete, unclear or non-existent.

Reference	Horizontal resolution (m)	Terrain model source	In-situ validation	Software
Present work	10	Airborne laser	3D sonic anemometers	OpenFOAM
Blocken et al. (2015)	10	Airborne imagery	2D sonic anemometers	ANSYS/Fluent
Bilal et al. (2016)	20	Not provided	Anemometers (unknown type)	WindSim
Tang et al. (2019)	Not provided	Not provided	cup anemometers	OpenFOAM
Barcons et al. (2018)	40	Not provided	3D sonic anemometers	Alya-CFDWind
Temel et al. (2018)	90	SRTM	2D sonic anemometers, weather balloons	OpenFOAM
Rasheed and Sørli (2013)	100	Not provided	None	SIMRA
Huang et al. (2018)	Not provided	SRTM	3D sonic anemometers	ANSYS/Fluent
Dhunny et al. (2017)	Not provided	Not provided	Anemometers (unknown type)	WindSim

structures (e.g. Burlando et al., 2007a). Among the mean flow characteristics evaluated in complex terrain, the mean AOA is rarely studied, even though its knowledge is fundamental to design properly a suspension bridge. Among the existing studies, Huang et al. (2018) classified the AOA with a histogram and bins of 5°, but estimates with higher accuracy are required for design purpose. Because the AOA requires the use of 3D sonic anemometers, it could not be assessed in Blocken et al. (2015) or Temel et al. (2018).

Therefore, the present study is unique in that it combines microscale flow simulation and full-scale measurements for wind engineering applications in complex terrain. The study aims to assess if and how 3D steady RANS simulation can be applied to improve the modelling of the mean wind conditions in a Norwegian fjord. The case of the Lysefjord is examined, the inlet of which is crossed by the Lysefjord suspension Bridge (N58°55′25.2″ E6°5′53.6″). The flow around the bridge has been monitored by 3D sonic anemometers since 2013 and by Doppler wind lidar instruments in 2014 (Cheynet et al., 2017b, 2016b). The inlet of the Lysefjord is modelled using a high-resolution DEM, computed from airborne laser measurements, with a horizontal spatial resolution of 10 m (Table 1). The mean flow characteristics relevant to wind engineering applications are simulated using the 3D steady RANS method and validated using velocity data collected in 2017 and 2018 from the nine sonic anemometers mounted above the bridge deck.

The paper is organized as follows: section 2 describes the full-scale measurement setup required for validation purpose. section 3 introduces the digital terrain model and the computational fluid dynamic model. This section also provides a convergence study and sensitivity study, focusing on the influence of the parameters used at the inlet boundary on the flow properties along the bridge deck. Section 4 compares the simulated mean flow characteristics with the in-situ data collected on the bridge between July 2017 and September 2018 for the two main wind sectors identified. The limits of semi-empirical approaches to modelling the topographical effects on the wind conditions at the bridge site are also briefly discussed in section 4.

2. Field measurements

2.1. Bridge instrumentation

The Lysefjord suspension bridge (Norway) has a main span of 446 m and is surrounded by mountains and steep hills that channel the flow. The distribution of wind directions on the bridge site is thus limited to the case of northeasterly flow, i.e. from the inside of the fjord, and a south-south-westerly flow, i.e. from the outside of the fjord. The localization of wind directions is demonstrated by the differences between Lysefjord Bridge and Sola Airport, located 27 km west from the bridge. A wind direction from northwest at the airport is generally linked to a flow from north-northeast at the bridge site (Fig. 2). When the wind blows from the southeast at Sola, a wind direction from south-southwest is recorded on the bridge.

The velocity data used herein were collected from multiple sonic anemometers installed 6 m and 10 m above the deck, i.e. approximatively 60 m above sea level (Fig. 3). The bridge girder has an asymmetric layout with respect to its midspan, associated with the 7.5 m altitude difference between the north and south end. The sonic anemometers were mounted on both sides of the girder and identified using the string HXY, where X is a digit between 08 and 24, corresponding to the hanger number, whereas Y refers to the west side (W) or east side (E) of the deck. Since two anemometers were mounted on the west hanger no. 08 (H08W), the notations H08Wb and H08Wt refer to the sonic anemometer mounted 6 m (bottom) and 10 m (top) above the deck, respectively. The distance between each hanger is 12 m, such that the anemometers monitored the flow along a 192-m line-segment parallel to the bridge axis.

Eight of the sonic anemometers were 3D WindMaster Pro from Gill instruments (Lymington, UK), which can operate with a sampling frequency up to 32 Hz. On H10W, a Weather Transmitter WXT520 from Vaisala (Helsinki, Finland) was deployed. In addition to being a traditional 2D sonic anemometer, this sensor can monitor rainfall, relative humidity, pressure and absolute temperature with a sampling frequency up to 4 Hz. A master data logging unit from CSI (Christchurch, New Zealand) synchronized the different sonic anemometers using GPS time, stored 10-min time histories into a single data file and continuously transmitted them, via a mobile network, to a server hosted by the University of Stavanger.

The velocity data considered hereafter correspond to stationary 10-min records, collected between July 2017 and September 2018. Before June 2017, the bridge was not instrumented with anemometers on both sides of the deck, which is important here for validation purpose. A similar dataset from 2017 to 2018 was also used to assess the flow characteristics around the bridge deck in Cheynet et al. (2019), which complements the present study. As the main focus here is on the mean flow characteristics, only the first-order stationarity of the time series was assessed, using a moving average filter with a window length of 5 min. Samples associated with instantaneous mean values that differ by more than 20% from the static mean were disregarded.

In the following, the along-wind, lateral and vertical velocity components are denoted u, v and w, respectively. The overbar denotes the temporal averaging such that the mean wind speed is written $\overline{u}$. The turbulence intensity I_i, where $i = \{u, v, w\}$ is defined as the ratio between the standard deviation of the component i and the mean wind speed. As reported by Cheynet et al. (2016a, 2019), the turbulence characteristics recorded on the Lysefjord Bridge depend strongly on the wind direction. The wind blowing from the inside of the fjord is often characterized by a unusually large turbulence intensity with $I_u \approx 23\%$ and $I_w \approx 17\%$. For a south-westerly wind, i.e. blowing toward the inside of the fjord, two distinct sub-sectors were identified. The first one is highly turbulent, with $I_u \approx 19\%$ (Cheynet et al., 2016b), with a mean wind speed $\overline{u} < 14$ m s^{-1}
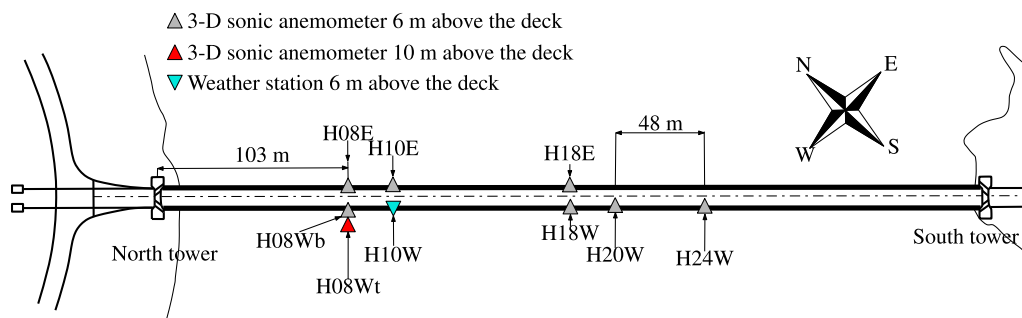
Fig. 2. Location of the sonic anemometers on the Lysefjord Bridge since July 2017.

and a wind direction between 175° and 195°. The second one corresponds to a lower turbulence intensity $I_u \approx 15\%$ and $I_w \approx 11\%$, associated with $\overline{u} > 14$ m s^{-1} and a wind direction between 210° and 230° at the bridge (Cheynet et al., 2016a). The corresponding wind direction at Sola airport is between 280° and 340°. At the bridge site, the ratio I_w / I_u ranges from 0.6 to 0.7 against 0.5 for flat terrains (Solari and Piccardo, 2001).

The influence of the atmospheric thermal stratification on the mean flow characteristics is not modelled in the following, which means the atmosphere is assumed to be neutral. The presence of steep hills and high mountains suggests that buoyancy-generated turbulence effects are not dominant in the flow (Cheynet et al., 2019). To dismiss as many samples characterized by non-neutral flow conditions as possible, those associated with a horizontal mean wind speed below 8 m s^{-1} are excluded from the analysis. For a flow from the inside of the Lysefjord, low-turbulent wind conditions with $I_u \approx 10\%$–12% and $\overline{u} \leq 10$ m s^{-1} were documented in Cheynet et al. (2017a) but are uncommon. These conditions correspond likely to a stable thermal stratification. Downslope flows have not been observed around the bridge, maybe because such events occur in wide fjords (Jackson and Steyn, 1994; Grønås and Sandvik, 1999; Oltmanns et al., 2014). Flow conditions characterized by an unstable stratification are not clearly distinguished from those corresponding to neutral conditions (Cheynet et al., 2019), which could be due to the numerous sea-land discontinuities around the bridge. For a wider fjord, strong wind events associated with non-neutral conditions may be studied more easily with dedicated codes, e.g. the WRF-LES model coupled with the immersed boundary method as by Arthur et al. (2018).

Among the flow characteristics studied, the mean AOA, denoted $\overline{\alpha}$, is defined as

$$\overline{\alpha} = \arctan\left(\frac{\overline{w}}{\overline{u}}\right) \tag{2}$$

where $\overline{w}$ and $\overline{u}$ are the vertical and horizontal mean wind velocity, respectively. The wind velocity is assumed to be an ergodic random process such that the ensemble average operator, which is used with the RANS method, is assumed to be well approximated by the temporal averaging used in full-scale. To simplify the comparison between the measured and simulated data, the mean wind speed along the bridge span is normalized by its value at mid-span. This normalization provides a non-dimensional velocity almost independent of the mean wind speed used at the inlet boundary condition (section 3.4).

2.2. Flow-distortion by the bridge deck

Although the anemometers are mounted several meters above the road, the velocity data recorded may not always be representative of undisturbed flow conditions because of the blocking by the bridge girder. The resulting flow distortion was documented in Cheynet et al. (2019) but is summarized herein for the sake of completeness.

Flow distortion is clearly visible in the vertical velocity component recorded by the anemometers located on the downwind side of the deck. Therefore, depending on the flow direction, the anemometers on the west side or the east side of the deck can measure a distorted flow. The mean AOA was found to be significantly underestimated by the anemometers located downwind. The fact that the vertical velocity component is more affected than the along-wind component by deck-induced flow distortion was also described by Hay (1984).

Following Jensen and Hjort-Hansen (1977) or Kristensen and Jensen (1979), the anemometers located upwind may overestimate the AOA. In Cheynet et al. (2019), for a south-westerly flow, the mean AOA recorded on H08Wt, 10 m above the deck, was in average 0.6° lower than recorded on H08Wb at 6 m above the deck. This value might be within the measurement uncertainty related to the levelling of the anemometers. Downwind, on H08E, the sonic anemometers recorded, on average, a mean AOA that was 1.7 lower than measured on H08Wt. The

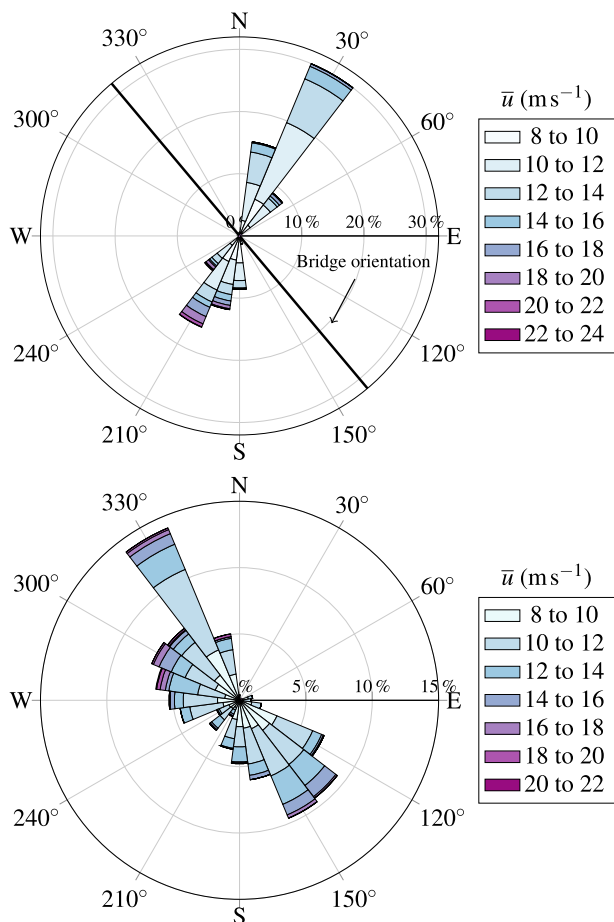**Fig. 3.** Wind rose corresponding to $\overline{u} > 8$m s^{-1} from the Lysefjord Bridge 60 m above sea level (top) and Sola airport, 10 m above ground (bottom), from July 2017 to September 2018.

anemometer located on H08Wt is at a distance equal to 3.6 H from the road, where H is the deck height. For a north-easterly flow, this anemometer is also affected by flow distortion, but to a lesser degree than the anemometers located 6 m, i.e. at 2.1 H above the road. Although an anemometer located 3.6 H from the road is much higher than usual, it is still possible that the anemometer on H08t record slightly overestimated AOA for a south-westerly wind. Therefore, the real AOA might be slightly lower than recorded by the anemometers located upwind but larger than the one recorded by the anemometer mounted downwind.

Deck-induced flow distortion was not found to significantly influence the mean wind speed and mean direction values along the span, in agreement with a pilot study using short-range wind lidar instruments to record the horizontal flow 40 m upstream of the deck (Cheynet et al., 2016b).

3. Numerical method

3.1. Terrain model

The choice of an appropriate terrain model is crucial to ensure a realistic flow simulation. In the present study, the digital elevation map is generated from airborne laser measurements, which have been exploited to establish a detailed national height model with a horizontal spatial resolution higher up to 1 m (Steiwer, 2017). The complete mapping of Norway should be achieved around 2020 but the elevation data already gathered are freely available (https://hoydedata.no/LaserInnsyn/). The area selected for the flow simulation is shown in Fig. 5 and is 8.5 km by 18 km with a maximum height of 650 m. The top of the computational domain is set to be five times the maximum height, i.e. 3.3 km. To reduce the computational cost, associated with the modelling of such a large domain, the horizontal resolution is set to 10 m. From the DEM, a ster-eolithography (STL) file is generated using Delaunay triangulation (Holcombe, 2011). The STL file is afterwards used to generate the un-structured Finite Volume computational mesh. The high resolution of the topography has the drawback to make the meshing algorithm numeri-cally unstable. This issue, already mentioned by Schmidli et al. (2018) for mesoscale flow simulation in mountainous environments, can be solved using a low-pass filter. To allow the meshing algorithm to converge while preserving the sharp slopes of the hills, a 2-D Gaussian smoothing kernel with a standard deviation of 0.25 is applied hereafter.

The wind direction near the Lysefjord Bridge results likely from a combination of main-valley and side-valley flows (Figs. 4 and 5). Main valleys are here defined as the fjord inlets, which are several hundred meters wide and covered by seawater. Side-valleys are generally nar-rower, sloppy, with heterogeneous topographic features and inclined toward the main valley such that side-valley flows mix with the main-valley flow. South to the Lysefjord Bridge, a 400-m high mountain (Fig. 4), named Uburen, could also influence the southerly flow recorded on the bridge. North to the bridge, a side valley (Fig. 5) may redirect a north-westerly flow into a north-easterly one. To account for the presence of various side valleys around the inlet of the Lysefjord, the computa-tional domain includes a fetch of 10 km to the south of the bridge and 8 km to the north.

The large turbulence intensity (TI) recorded on the Lysefjord Bridge for some wind directions suggests that side-valley dominated flows are more turbulent than those following the main-valleys. This assumption is used herein to compare the measured and simulated flow characteristics. Samples associated with a TI for the along-wind component above or equal to 20% are suspected to be representative of side-valleys domi-nated wind conditions. Such high turbulence intensities were reported in Cheynet et al. (2019) for a flow from north-northeast, which suggested that the upstream flow was too turbulent to be governed by the chan-nelling effect of the fjord. On the other hand, a TI below 15% could be associated with main-valley dominated flow, as similar values were recorded on other fjord-crossing bridges (Kristensen and Jensen, 1979; Fenerci, 2018). Samples with a TI between 15% and 20% could

Fig. 4. Top panel: Uburen seen from the northern side of the Lysefjord Bridge. Bottom panel: Lysefjord Bridge seen from the top of Uburen.

correspond to more equal mixing between main valleys and side valleys but are not considered in the following.

The northern wind sector is defined here as the range of wind di-rections spanning from northwest to northeast. For this sector, the wind direction recorded by the anemometers on the bridge is between 15° and 35° for both high and low-turbulent conditions. According to a private weather station located at Idse, ca. 13 km north-west to the Lysefjord Bridge, the most common wind directions in the northern sector range from 330° to 340°. Therefore, the initial wind direction of 335° is selected as a first case study. To generate a northerly flow following the main valley, a wind direction of 355° is selected as a second case study. If the flow is simulated from the inside of the fjord (not shown here), i.e. with initial wind directions between 50° and 60° at the inlet, the asso-ciated wind direction along the bridge span is larger than observed in full-scale. Note that seven initial wind directions between 330° and 355° were investigated for the northerly sector but only two of them are considered (Table 2) as the other ones did not show substantial differences.

For the southern sector, the velocity records showed that a TI above 20% was recorded for a wind direction below 190°, which could be simulated considering a wind blowing from 168° at the inlet boundary, i.e. almost parallel to Høgsfjord (Fig. 5). A TI below 15% was associated with an average wind direction of 210°, which is the most common one recorded for the southern sector (Fig. 2). This wind direction was reproduced by simulation using a flow direction of 210° at the inlet boundary. For the southern sector, nine different wind directions be-tween 155° and 210° were actually simulated but only two of them are
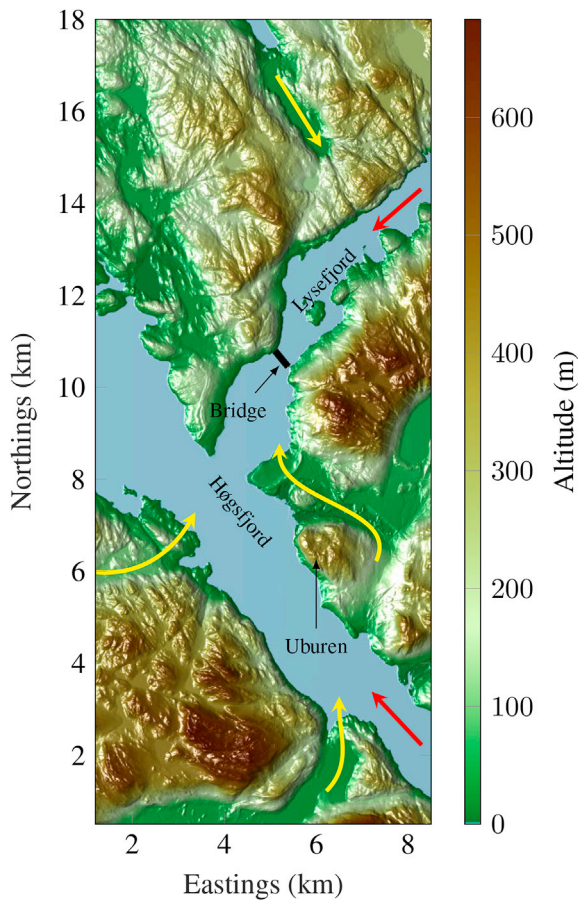
Fig. 5. Digital elevation map used to generate the computational domain around the Lysefjord bridge, with expected main-valley flows (red arrows) and side-valley flows (yellow arrows).

discussed here for the sake of brevity.

To improve the confidence in the simulated flow characteristics, in-situ measurements can be used to specify or update some of the initial or boundary conditions. This approach, called "data assimilation" was initially developed for numerical weather prediction softwares (Kalnay et al., 1996). In the Lysefjord, all the anemometers are located along the bridge deck, which is not suitable for an efficient application of data assimilation techniques. For optimal performances, the sensors would need to be several kilometres from each other. In addition to the increased numerical cost, the use of data assimilation in complex terrain is challenging (Bilal et al., 2016; Hacker et al., 2018). Nevertheless, it deserves further attention for its potential in modelling storm events for wind engineering applications.

3.2. Roughness length

In the present model, wall functions are used at the lower boundary. Therefore, a roughness length representative of the local terrain needs to

Table 2
The four different cases investigated for the microscale CFD simulation in the Lysefjord, where $(z_0)_i$ and $\bar{u}_{ref}$ are the roughness length value and the reference mean wind speed at the inlet boundary, respectively.

Direction at the inlet	$\bar{u}_{ref}$ (m s^{-1})	z_{ref} (m)	$(z_0)_i$ (m)
168°	10	60	0.05
210°	10	60	0.05
335°	10	60	0.3
355°	10	60	0.3

be specified. The roughness length models the effect of obstacles on the flow (Davenport, 1961; Wieringa, 1993) but not flow detachments or recirculation zones induced by steep slopes. By definition, the DEM used herein does not include vegetation and buildings as only a Digital Surface Model (DSM) offers this possibility. However, a DSM can be a source of numerical instabilities as the terrain model is rougher. Therefore, establishing a relevant roughness length for a narrow Norwegian fjord is challenging as both the terrain slopes and the local roughness need to be modelled. The heterogeneity of the terrain, leading to multiple internal boundary layers, can be described using a roughness map (Astrup et al., 1997; Petersen et al., 1998), which classifies the land cover using a local roughness length value.

The use of a roughness map implies that the parameter z_0 in eq. (11) is no longer a scalar but a function of the tile coordinates. Roughness maps are commonly used for wind resource assessment (Petersen et al., 1998; Lange and Højstrup, 2001) and are traditionally established trough satellite, aerial and ground-based images. The absence of a database to establish a roughness map for the Lysefjord is circumvented by computing a local roughness length using the two-dimensional gradient of the terrain height with a horizontal resolution of 10 m. This method is highly effective to distinguish between water areas (sea or lake) and land areas. The resulting roughness is likely more heterogeneous than in reality. Therefore, the roughness map is smoothed using a 2-D Gaussian smoothing kernel with a standard deviation of 2, producing the map displayed in Fig. 6. The classification into five terrain categories is done using the inclination angle i

$$i = \arctan\left(\frac{d_z}{H}\right) \tag{3}$$

where $H = 10$ m is the horizontal resolution and d_z is the local terrain gradient.

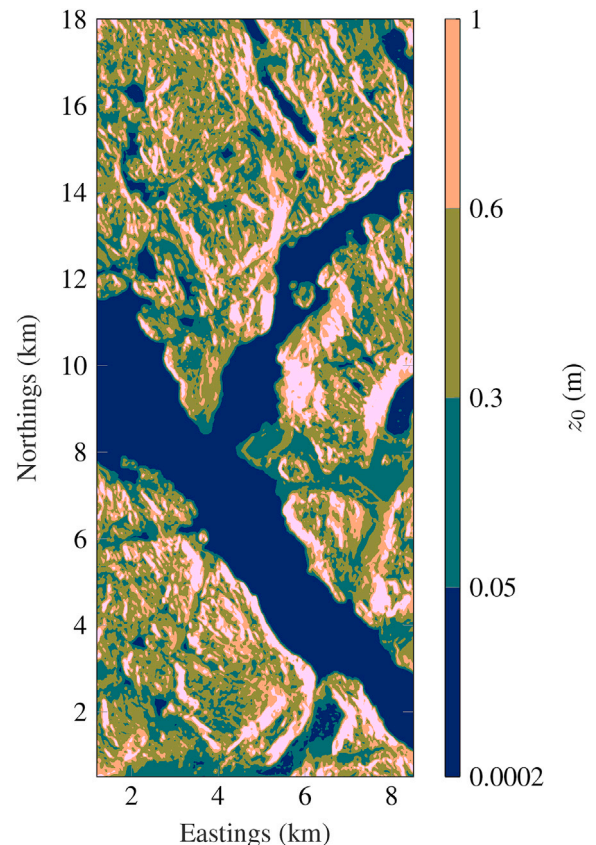The choice of roughness length into five terrain categories (Table 3) is

Fig. 6. Roughness map of the computational domain.

Table 3
Local roughness length defined using the local terrain gradient.

Inclination angle i (°)	d_z (m)	z_0 (m)
$i < 0.03$	$d_z < 0.006$	0.0002
$0.03 \leq i < 6$	$0.006 \leq d_z < 1$	0.05
$6 \leq i < 17$	$1 \leq d_z < 3$	0.3
$17 \leq i < 27$	$3 \leq d_z < 5$	0.6
$i \geq 27$	$d_z \geq 5$	1

Table 4
Mesh size tested for the convergence study.

Mesh name	Southeast sector				Northwest sector			
	A	B	C	D	A	B	C	D
Number of cells ($\cdot 10^6$)	21.1	15.0	7.0	3.7	21.1	15.0	7.0	3.1
Largest cell (m)	54	60	80	100	54	60	80	108
Cell size at ground level (m)	0.8	0.8	1	1	0.8	0.8	1	1
Cell size at bridge level (m)	18	20	27	33	18	20	27	36
Computational time (h)	18	12	5	3	17	12	5	2

done following Wieringa (1993) and EN 1991-1-4 (2005). The lowest value $z_0 = 0.0002$ m concerns water areas. The second value $z_0 = 0.05$ m corresponds mainly to agricultural crops on flat terrains. A slightly larger inclination angle is associated with hills covered by bushes, forests and/or low buildings for which two different roughness lengths have been defined: $z_0 = 0.3$ mand $z_0 = 0.6$ m. The highest level of roughness described here, for which $z_0 = 1$ m, corresponds to cliffs, escarpments or hills with steep slopes.

3.3. Computational fluid dynamic approach

The finite-volume based CFD method is used within the OpenFOAM software (Jasak, 2009) to solve the incompressible 3D steady RANS equations. The governing equations consist of the momentum conservation equation:

$$\nabla \cdot (\mathbf{uu}^T) - \nabla \cdot [\nu \nabla \mathbf{u} + \mathbf{R}] = -\frac{1}{\rho}\nabla p \tag{4}$$

and the continuity equation:

$$\nabla \cdot \mathbf{u} = 0. \tag{5}$$

Here, $\mathbf{u}$ is the velocity field, ν is the kinematic molecular viscosity, $\mathbf{R}$ is the Reynolds stress tensor allowing general turbulence modelling, ρ is the density field and p is the pressure field.

Turbulence is modelled using a realisable k–ε model (Shih et al., 1995), which is appropriate for high-Reynolds number flows (Lun et al., 2003). The discretisation of the convection term, i.e. the first term in eq. (4), is performed using a limited, implicit, second-order central differencing scheme, which is a Galilean invariant version of the Gamma scheme proposed in Jasak et al. (1999). The second term, which is the diffusion term, is discretised using an implicit linear scheme. The right-hand term of eq. (4), i.e. pressure gradient, is discretised using an explicit linear scheme. The convection terms of the dissipation rate of turbulent kinetic energy ε and the turbulent kinetic energy k are discretised using an implicit first-order upwind scheme. The Laplacian pressure operator arising from the continuity equation is discretised using a linear scheme with explicit limited non-orthogonal correction.

3.3.1. Computational grid and boundary conditions

The computational grid is generated as an unstructured, body-fitted Finite Volume grid, using the software called cfMech (F. Juretić, 2017).

The mesh in areas of high interest, i.e. near the terrain and near the bridge, is refined while it gets coarser towards the top of the domain. Since coupling mesoscale and microscale flow simulations is out of the scope of the present work, the boundary conditions are defined using realistic values supported by in-situ measurements, as shown herein.

For the inlet boundary: a fixed value is used for the vertical mean wind speed profile following the modified law of the wall proposed by Hargreaves and Wright (2007). A normal zero-gradient boundary condition is imposed for the pressure, whereas fixed-value boundary conditions are used for the turbulence variables k and ε (Richards and Hoxey, 1993):

$$k = \frac{(u_*)^2}{\sqrt{C_\mu}}, \tag{6}$$

$$\varepsilon = \frac{(u_*)^3}{\kappa(z + (z_0)_i)}, \tag{7}$$

where u_* is the friction velocity; $\kappa = 0.41$ is von Kármán's constant, $C_\mu = 0.09$ is the turbulence viscosity coefficient, z is the vertical coordinate and $(z_0)_i$ is the surface roughness length at the inlet boundary. The roughness length parameters are chosen based on the available information on the typical TI for the two main wind directional sectors studied. The roughness length $(z_0)_i$ is set equal to 0.05 m for the flow from south of the bridge, which corresponds to a terrain category II in the Eurocode (EN 1991-1-4, 2005). For a flow from the inside of the Lysefjord, $(z_0)_i$ is set equal to 0.3 m, as suggested for a terrain category III in the Eurocode to account for the more heterogeneous topography.

The friction velocity at the inlet boundary is computed assuming a logarithmic vertical profile for the mean wind speed:

$$u_* = \kappa \frac{\overline{u}_{ref}}{\ln\left(\frac{z_{ref} + (z_0)_i}{(z_0)_i}\right)}, \tag{8}$$

where $\overline{u}_{ref} = 10$m s^{-1} is the reference wind speed at the reference height $z_{ref} = 60$ m. Therefore, the computed friction velocity is equal to 0.56 m s^{-1} for $(z_0)_i = 0.05$ m and 0.75 m s^{-1} for $(z_0)_i = 0.3$ m. The sea state around the bridge is assumed calm due to the sheltering effect of the valleys and islands, but also the change of fjord orientation south of the bridge. However, for a wider and more open fjord, the dependency of the roughness length on the sea state and fetch (Charnock, 1955) needs to be accounted for.

For the outlet boundary, a normal zero-gradient condition is set for the velocity, while a fixed value atmospheric pressure is imposed for the pressure variable. For the backflow at the outlet boundary, the velocity is locally set to zero. An equivalent boundary condition is set for turbulence variables k and ε, namely normal zero-gradient for out-flowing velocity and a fixed value of zero for the backflow;

For the top boundary, a free boundary condition is set for the velocity, allowing the flow to go in and out freely. The pressure is described by subtracting the dynamic pressure from the total pressure, i.e., $p = p_0 - 1/2|\mathbf{u}|^2$, where p_0 is total pressure and $\mathbf{u}$ is the velocity vector at the top boundary. For k and ε, a normal zero-gradient is applied to the out-flowing velocity and a zero fixed value is set for in-flowing velocity;

For the terrain, a no-slip condition is set for the velocity, i.e. a zero fixed value condition, and a normal zero-gradient condition is set for pressure. For the cell adjacent to the wall, denoted by the subscript p, the variables ε_p and k_p are computed using wall function approximations:

$$k_p = \frac{(u_*)^2}{\sqrt{C_\mu}}, \tag{9}$$

$$\varepsilon_p = \frac{(u_*)^3}{\kappa z_p},\tag{10}$$

where z_p is the normal distance from the wall to the first cell centroid away from the wall. In the cell adjacent to the wall, the turbulent viscosity ν_T, contained in the Reynolds stress tensor $\mathbf{R}$, incorporates a local roughness length z_0:

$$\nu_T = \kappa \frac{u_* z_p}{\ln\left(\frac{z_p + z_0}{z_0}\right)} - \nu.\tag{11}$$

3.4. Convergence and sensitivity study

For the sake of simplicity, the simulated flow is examined from now on in a horizontal plane 60 m above sea level, which corresponds roughly to the altitude of the anemometers. Four different mesh configurations, denoted by the letter A to D, are investigated to assess the dependency of the simulated flow characteristics on the computational grid (Table 4). The convergence study is conducted using a uniform roughness length with the same value at the inlet boundary and inside the computational domain. The simulation is conducted using the Vilje supercomputer (https://www.sigma2.no/content/vilje) with a 2.6-GHz Intel CPU and 192 cores. A different mesh is generated for each wind direction. Therefore, the sensitivity of the mean flow characteristics on the computational grid is illustrated hereafter for a northeast and southeast flow. Fig. 7 indicates that, along the bridge deck, meshes A to C provide similar results for the two selected wind sectors. For the northeasterly direction, mesh D, which has the least number of cells and the largest cell size, fails to capture the recirculation zone on the northeast side of the bridge, leading to an erroneous wind direction at the bridge site. The consistent flow characteristics obtained with meshes A, B and C may partly be due to the similar cell size at the deck height. Nevertheless, the large spatial dimension of the domain implies that the total number of cells varies considerably between mesh C (7 million cells) and mesh A (21 million cells). In the following simulations, the grid resolution corresponding to mesh B is used.

3.4.1. Influence of the roughness length at the inlet boundary

In the case of a wind direction equal to $335°$, the influence of $(z_0)_i$ on the simulated flow characteristics at the fjord inlet is investigated using first $(z_0)_i = 0.3$ m and then $(z_0)_i = 1$ m. In both cases, the roughness of the computational domain is either defined as uniform, with values equal to $(z_0)_i$ or heterogeneous with values given by the roughness map defined in section 3.1. For a southern flow with a direction of $168°$ at the inlet boundary, a single roughness length $(z_0)_i = 0.05$ m is used. The flow characteristics along the bridge deck associated with these different scenarios are summarized in Fig. 8. The use of a roughness map generates numerous internal boundary layers, which may explain why the influence of the value of $(z_0)_i$ on the simulated flow characteristics is considerably reduced when the roughness map is used. For a northern flow, the use of a uniform roughness length leads to a clear dependency of the mean wind direction along the bridge on the roughness length value at the inlet boundary. These results justify the use of a roughness map as a way to diminish the influence of the boundary conditions on the simulated flow characteristics. Interestingly, the case of a southern flow shows that the use of a roughness map has limited effects on the flow characteristics along the bridge.

3.4.2. Influence of the mean wind speed at the inlet boundary

The influence of the mean wind speed at the inlet boundary on the flow characteristics along the bridge deck are evaluated for the case of a wind direction of $168°$ at the inlet. Four different initial mean velocities, with values of 5 m s^{-1}, 10 m s^{-1}, 18 m s^{-1} and 30 m s^{-1} were considered. Fig. 10 shows that the along-span profile of the mean flow characteristics is almost independent of the mean wind speed used at the inlet, except for $\bar{u} = 5$ m s^{-1}. This indicates also that the simulated flow for low inlet wind speeds, such as 5 m s^{-1}, may to a greater extend go around the hills and mountains rather than over them, resulting in a flow pattern that has a more southerly wind direction along the bridge. Using full-scale records from the sonic anemometer on H18W, the bivariate histogram of the wind speed and wind direction at the bridge site is displayed in Fig. 9. Whereas records associated with a direction of ca. 180 are among the most commonly observed at the bridge site, they become almost inexistent for a mean wind speed larger than 11 m s^{-1}, which is consistent with the middle panel of Fig. 10. In section 4, only the case of a mean wind speed of 10 m s^{-1} at the inlet is considered, especially since it is more frequently recorded by the anemometers on the bridge, compared to higher mean wind speeds of interest.

4. Results

4.1. Case of a southerly flow

South of the bridge, two cases are investigated. The first one corresponds to a wind direction of $168°$ at the inlet (Fig. 11), leading to a flow
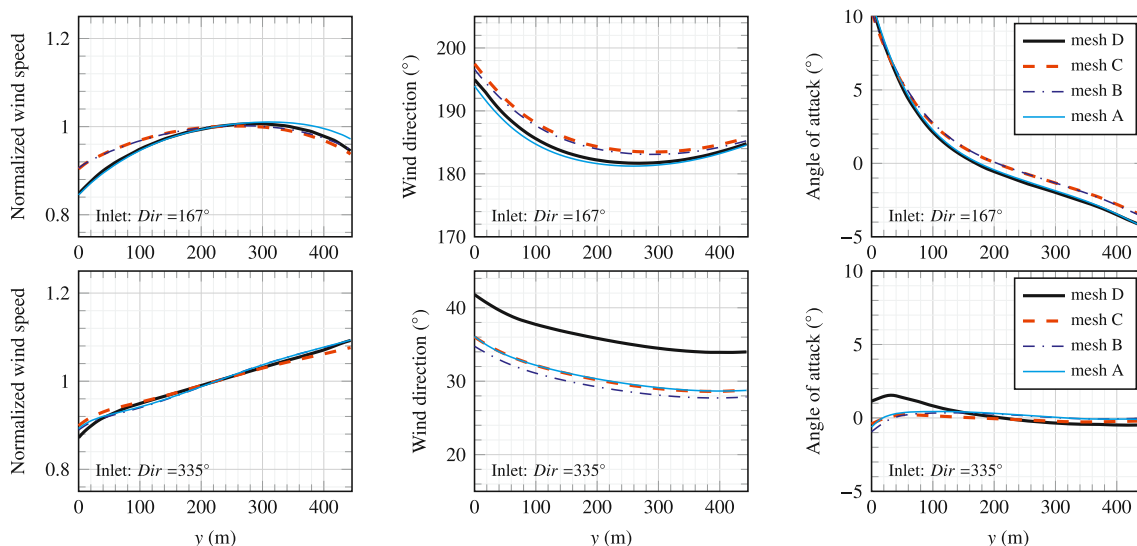

Fig. 7. Mean flow characteristics simulated along the bridge deck from the bridge north tower ($y = 0m$) to the south tower ($y = 446m$) for four different mesh cases (Table 4). The wind direction at the inlet is $168°$ (top panels) or $335°$ (bottom panels).
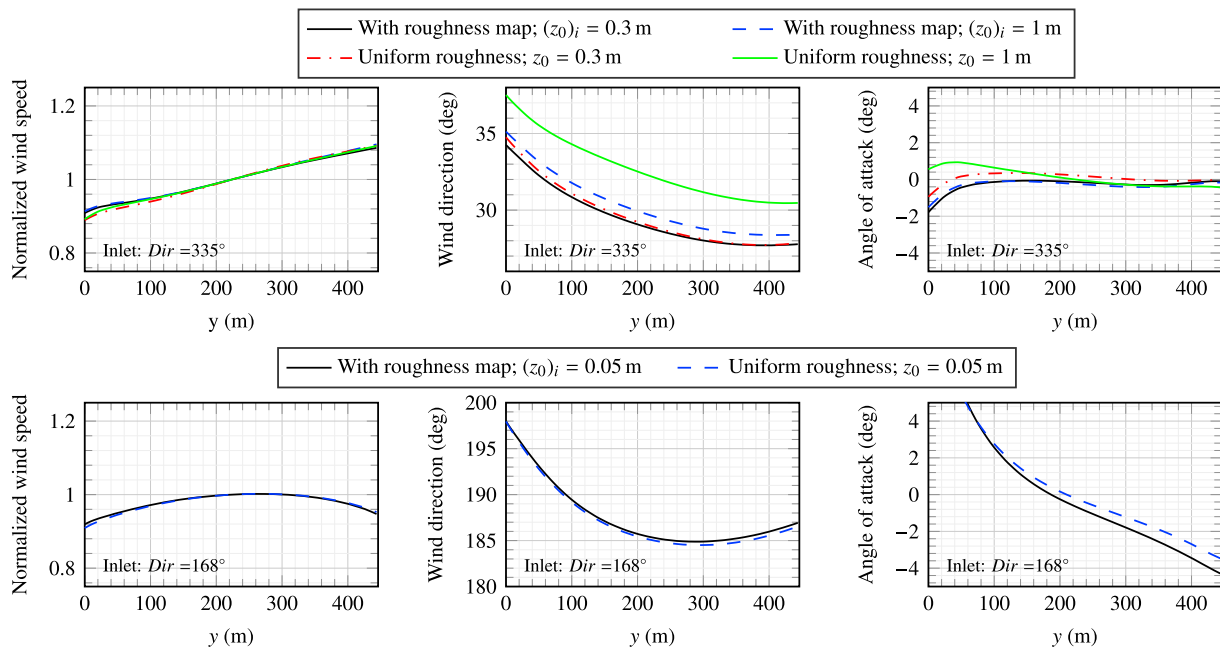
Fig. 8. Mean flow characteristics simulated at the inlet of the Lysefjord with and without roughness map, for a northerly flow (top panels) and southerly one (bottom panels).

following the main fjord (Høgsfjord) as suggested by the weather station at Idse. This flow combines with another one from a side-valley, approximatively 6 km south of the bridge, captioned "1st merging" in Fig. 1. North of the mountain named Uburen, a second side-valley flow merges partially with the one from the main valley, captioned "2nd merging" in Fig. 11. However, at the deck position, the side-valley flow seems to dominate over the one from the main valley. Fig. 11 shows that the flow entering the Lysefjord emerges from a small side valley, north of Uburen, rather than from the main fjord. The second case examined corresponds to a south-westerly wind direction of 210° at the inlet (Fig. 12), for which the flow from the side valley is no longer dominating at the fjord inlet.

Fig. 13 compares the measured and simulated mean flow characteristics along the bridge associated with an initial direction of 168° and 210°. The full-scale records selected for comparison with the case where the side-valley flow is dominating are those associated with a TI above
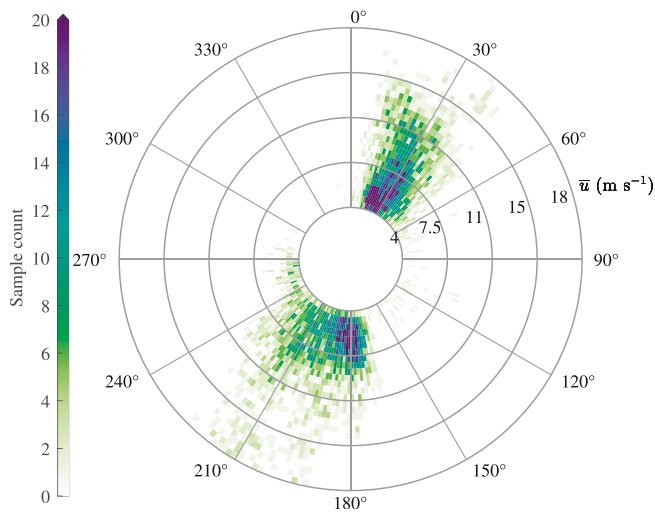

Fig. 9. Histogram of the mean wind speed as a function of the wind direction using records from the Lysefjord Bridge, at midspan, between July 2017 and September 2018.
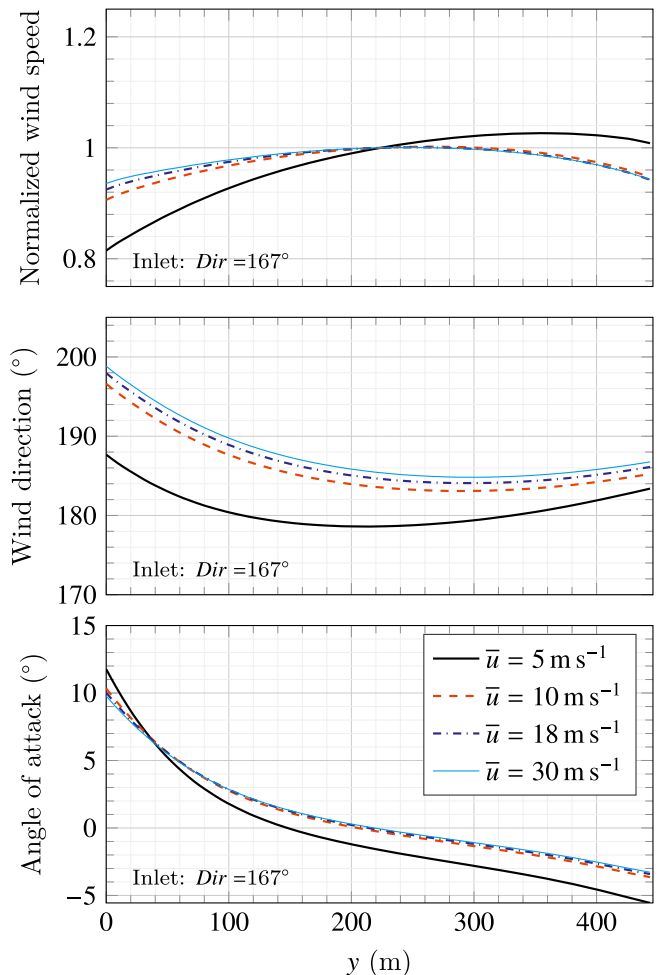

Fig. 10. Mean flow characteristics simulated along the bridge deck for the mesh B, with different mean wind speed and a direction of 168° at the inlet.
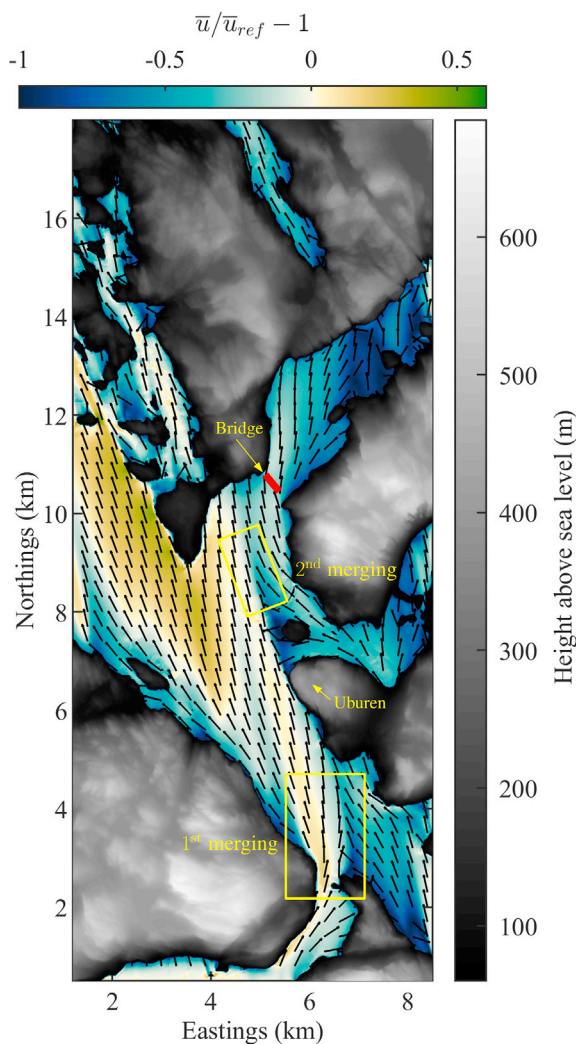
Fig. 11. Normalized mean horizontal wind velocity 60 m above the surface, simulated with a direction of 168° at the inlet boundary.

Fig. 12. Normalized mean horizontal wind velocity 60 m above the surface, simulated with a direction of 210° at the inlet boundary.

20% for the southerly flow. Samples compared to the case of a dominating main-valley flow are those associated with a TI below 15%. The good agreement between the measured and simulated mean wind directions shows that the inlet boundary conditions are realistic and that the interactions between the side-valley flow and the main-valley flow have a substantial impact of the wind characteristics recorded on the bridge deck.

When the flow from the main valley is dominating, the computed AOA is positive along the bridge and fairly uniform. The positive AOA observed for the southern flow is attributed to the abrupt narrowing of the fjord as the flow approaches the bridge. If the flow from the side valleys dominates, the AOA is non-uniform along the bridge span, illustrating the complex interaction between side-valleys and main-valley flows. In both cases, the simulated AOA underestimates the measured one by approximatively 1° if the inlet wind direction is 168° and by 2°–3° if the wind direction at the inlet is 210°. In summary, the CFD simulation captures fairly well the along-bridge variation of the AOA. It is observed for the full-scale results that the sensors H08E, H10E and H18E, which are located downwind, give a lower AOA than the sensors located on the windward side. This is likely related to blockage effects caused by the girder as the flow passes over the deck.

The results shown in Fig. 13 reinforce the idea that if the wind direction recorded at the bridge site is below 190°, the dominating part of the flow comes from a side-valley, linked to the larger TI recorded by the
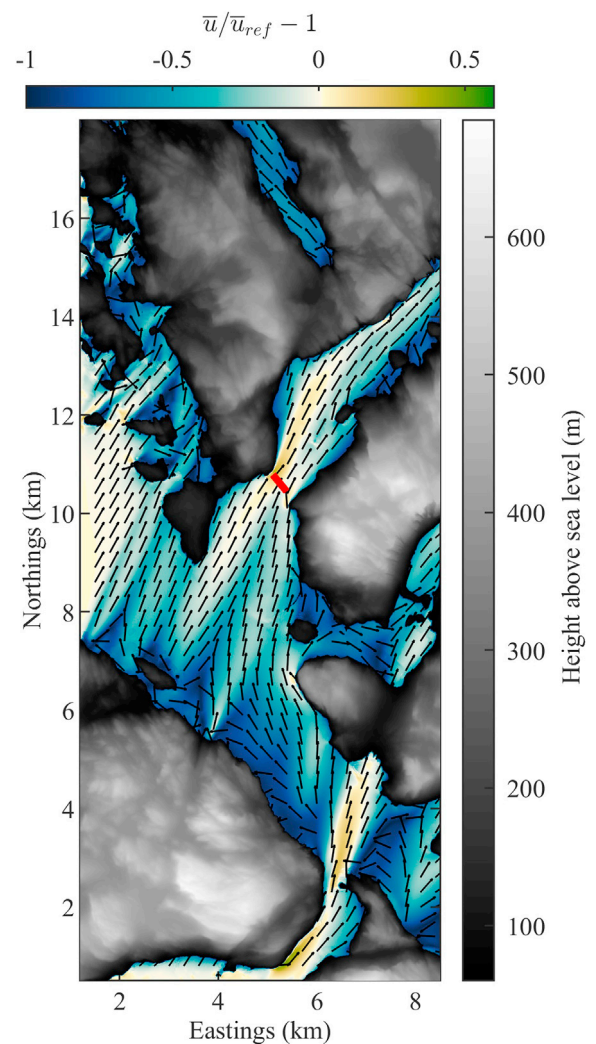
anemometers. Although the mean wind speed seems fairly uniform along the deck, a larger velocity gradient is observed near the south tower. It is not possible to conclude whether this flow heterogeneity is realistic because of the lack of measurements near this location.

A similar flow analysis was also done using a different terrain model, namely the SRTM dataset with a horizontal resolution of 30 m and wind directions at the inlet of 210° and 170°. In terms of AOAs and along-span wind direction, a better agreement was obtained than with the more detailed terrain model considered in the present study. On the other hand, the SRTM terrain model did not lead to a significant improvement of the along-deck profile of the mean wind speed. A detailed comparison of digital terrain models for microscale flow simulation is out of the scope of the present work. Nevertheless, the flow analysis with the SRTM terrain model suggests that a horizontal resolution higher than 30 m may not necessarily lead to more realistic flow characteristics in a narrow Norwegian fjord. This is an important finding because the SRTM dataset has a global coverage, at latitudes between −54° and 60° (Van Zyl, 2001). Unfortunately, only a small fraction of Norway is located at latitudes below 60°, which limits the applicability of the SRTM terrain model to study the wind conditions in Norwegian fjords.

It should be noted that the inlet of the Lysefjord is not a straight channel, so the maximum wind speed is not reached on its middle but close to the inside of the curvatures, as it would be for a curved-channel flow. The interactions between side-valley and main-valley flow can also
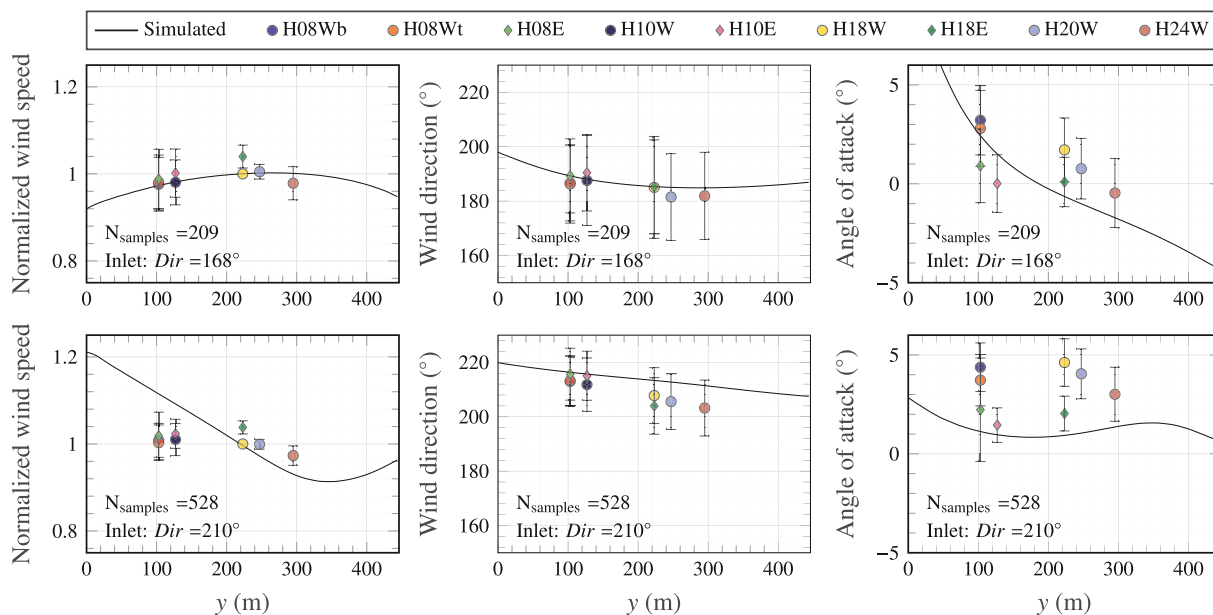
Fig. 13. Simulated (solid lines) and recorded (scatter plot) mean flow characteristics along the bridge for a southerly wind dominated by a side-valley flow (top panels) and one by the main valley flow (bottom panels). The error bar corresponds to two standard deviations from the mean value and $N_{samples}$ is the number of 10-min records selected for comparison.

disturb the homogeneity of the upstream flow. Therefore, the across-fjord profile of the mean wind speed cannot be symmetric to the middle part of the bridge span. The use of Doppler wind lidar near the bridge in Cheynet et al. (2017b) showed, for example, a maximal speed at the southern end of the bridge for a wind blowing from south-southwest.

4.2. Case of a northerly flow

In Fig. 14, the flow simulated with an initial wind direction of 335° propagates toward the bridge mainly through a side valley. This results in a recirculation zone approximatively 2 km north-east to the bridge, located at the junction between the side-valley and the Lysefjord. The two valleys merge with an angle close to 90°, which prevents the flow inside the fjord from reaching the bridge. A recirculation zone is generally defined as a stationary vortex where the flow direction becomes reversed, but in Fig. 14, such a vortex is located in a horizontal plane. The unusually high TI recorded on the northern side of the bridge may partly be due to the presence of this recirculation zone. This speculation is conceivable as a recent study in complex terrain by Menke et al. (2019) using Doppler lidar technology showed that recirculation zones can be locally responsible for a considerable increase of the TI. On the other hand, in Fig. 15, the flow with a wind direction of 355° does not clearly show any interactions between the flow from the side-valley and the one following the main-valley. In this situation, the wind conditions recorded at the bridge site seem to correspond to a flow following the fjord. The lack of recirculation effects may be linked to uncommon events where a low TI was recorded at the bridge site (Cheynet et al., 2017a).

Fig. 16 compares the measured and simulated mean wind characteristics for the two northerly wind directions selected. It should be noted that the samples chosen for comparison with the side-valley dominated flow are those with a TI above 20% at midspan, whereas the samples with a TI below 15% are assumed to be associated with a flow following the main valley. For both simulated cases, the flow entering the side valley from the north-west follows the changing orientation of the passage into the fjord and crosses the bridge from north-east (Fig. 14). This results in similar wind directions at midspan, between 20° and 35°. Therefore, for the northerly flow, the wind direction alone cannot be used to distinguish records representative of a side-valley or the main-valley flow. The discrepancies observed for the normalized mean wind speed profile and the

AOA shows that considering only the mean flow properties may not be sufficient to assess whether the highly turbulent north-east flow recorded on the bridge is linked to the recirculation zone.

When the wind recorded on the bridge deck comes from the inside of the fjord, the anemometers located on the west side of the girder can be affected by the deck-induced flow distortion, discussed in section 2.2. This leads to an underestimation of the AOA, as shown by the sensors on H08Wb and H08Wt in Fig. 16. The large standard deviation associated with the data recorded by the anemometer on H18E suggests that this sensor is not as reliable as the others. An additional source of scattering for the AOAs is the possible imperfect levelling of the anemometers above the girder. For the flow conditions considered, the limited number of non-neutral conditions recorded is not expected to significantly affect the AOA.

The somewhat poorer comparison between the simulated and measured flow characteristics for the northerly flow compared to the southerly flow is perhaps linked to the choice of the computational domain. The distance from the northerly inlet boundary conditions to the bridge location may not allow a realistic interaction between the flows from different valleys. Therefore, extending the computational domain on the north-east of the bridge to better capture the flow coming from the inside of the Lysefjord may lead to an improved comparison between the simulated and measured flow characteristics. It should also be noted, that the atmospheric thermal stratification was not accounted for in the present study, even though the low-turbulence intensity measured for a north-easterly wind is likely associated with stable flow conditions (Cheynet et al., 2017a).

4.3. Limits of the semi-empirical topographic models

The possible interactions between main-valley and side-valley flows, highlighted for both a southerly and northerly wind at the inlet of the Lysefjord cannot realistically be predicted by the semi-empirical modelling of topographic effects. The Norwegian annexe in EN 1991-1-4 (2005) provides both a turbulence factor and a topography factor, which can be used to compute the TI while accounting for the presence of hills and ridges upstream to the structure studied. However, in such a model, the flow is assumed to be unidirectional, which prevents an accurate estimation of the equivalent upstream roughness length and,
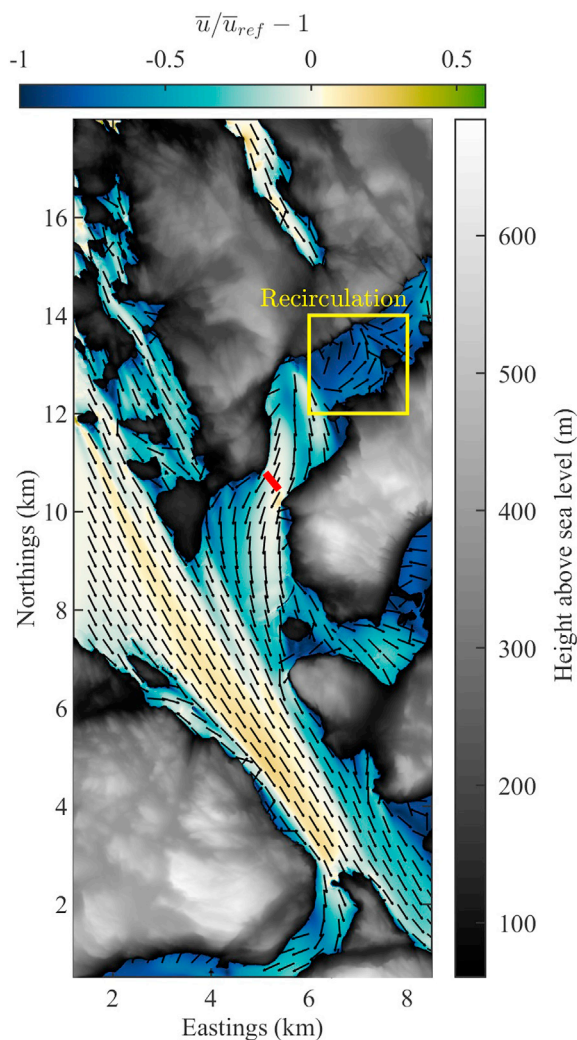
Fig. 14. Normalized mean horizontal wind velocity 60 m above the surface, simulated with a direction of 335° at the inlet boundary.

Fig. 15. Normalized mean horizontal wind velocity 60 m above the surface, simulated with a direction of 355° at the inlet boundary.

therefore, the TI at the deck location.

The standard ESDU 01008 (ESDU, 2001) provides estimates of the local roughness value and friction velocity in hilly terrains based on the model from Deaves (1981). While the ESDU 01008 attempts to capture three-dimensional effects of hills, it does not account for local changes of the wind direction. Therefore, in the case of a wind direction of 30° at the Lysefjord Bridge deck, the equivalent roughness length at the deck position was only around 0.03 m because the total fetch corresponding to the water area is overestimated.

The application of CFD micro-scale flow simulation in the design stage of a fjord-crossing bridge is relevant to identify situations were side-valley flow are dominating, which may be associated with unusually large turbulence intensities, which are not well predicted by semi-empirical topographic models. Validation of CFD simulations by in-situ measurements might be achieved using anemometers on masts installed on the shore of fjords of interest, like those installed in the Bjørnafjord (Cheynet et al., 2018) or Sulafjord (Wang et al., 2019) since 2015.

5. Conclusions

The influence of the local topography on the mean wind conditions recorded at the inlet of a narrow fjord, called Lysefjord, has been investigated by combining 3D steady Reynolds-averaged Navier-Stokes simulation with in-situ measurements from 3D sonic anemometers. The
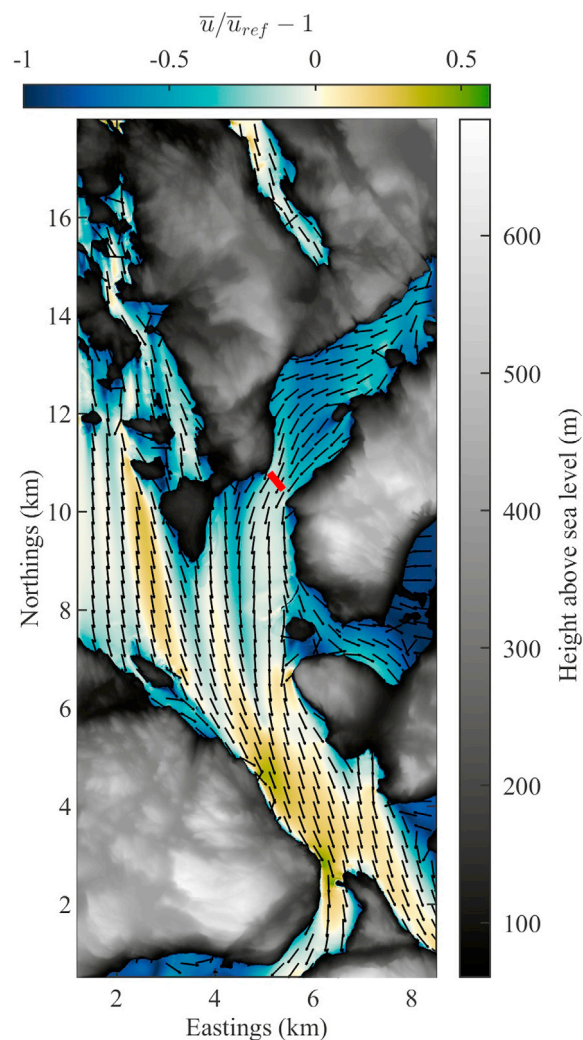
complex topography is modelled using high-resolution airborne laser measurements, which provided a digital elevation map with a horizontal resolution of 10 m. The flow features investigated are the uniformity of the mean wind speed and direction, as well as the angle of attack along the bridge main span. All are relevant for modelling the wind load on long-span bridges. The first objective is to better understand the complex flow conditions recorded along the Lysefjord Bridge. The second objective is to explore if and how microscale CFD simulations can be used to improve the design basis for future bridges crossing a fjord or a valley. The comparison between simulated and observed wind characteristics leads to the following findings:

- Side valleys may have a major influence on the wind conditions recorded along the bridge deck. More precisely, the full-scale wind records suggest that an unusually high turbulence intensity is linked to flow driven by one or multiple side valleys. The application of the high-resolution steady 3D RANS method provides valuable information on the flow features in complex terrain. In particular, for the design phase of a bridge, it can help to predict quantitatively whether a given wind sector may be associated with a non-uniform or non-horizontal flow and/or a local increase of the turbulence intensity.

- The comparison between the full-scale and simulated wind characteristics shows that in complex terrain, 3D sonic anemometers are essential for validation purpose as the flow may no longer be horizontal. In particular, the positive angles of attack recorded from the
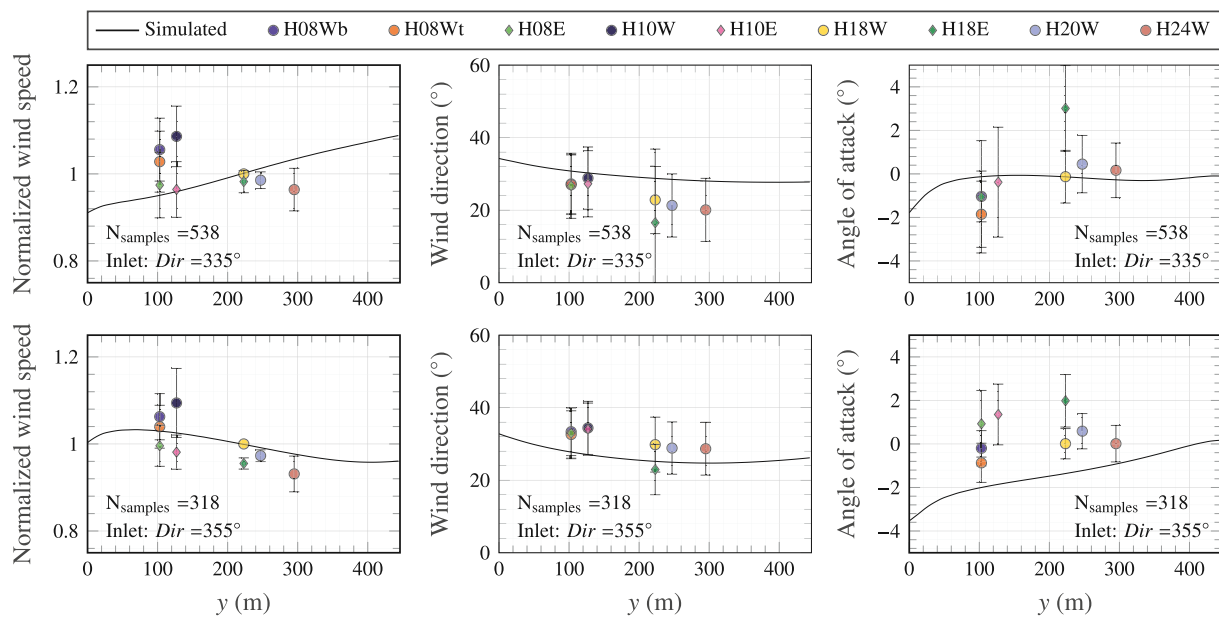
Fig. 16. Simulated (solid lines) and recorded (scatter plot) mean flow characteristics along the bridge for a wind direction at the inlet boundary of 335° (top panels) and 355° (bottom panels). The error bar corresponds to two standard deviations from the mean value and $N_{samples}$ is the number of 10-min records selected for comparison.

bridge with values between 2° and 5°, which are observed for a south-south-westerly direction, are partly supported by the simulated data.

- Both the simulated and measured mean wind speeds were relatively uniform along the bridge deck, with fluctuations of ± 10% around the value at mid-span. Therefore, in the case of the Lysefjord Bridge, the assumption of uniform mean wind speed along the deck seems acceptable. The simulated wind direction increases toward the north tower, in agreement with the in-situ measurements, with a difference up to 15° between the two extremities of the main span.

- The choice of an appropriate roughness length is a major challenge for realistic flow simulation in a narrow fjord. In the present case, a local roughness length is modelled using a roughness map, which significantly reduces the influence of the roughness length value at the inlet boundary on the mean flow properties at the bridge site.

The application of the 3D steady RANS method for microscale wind simulations complemented by in-situ measurements and wind tunnel tests may provide valuable knowledge on the local wind conditions and help to establish an improved design basis for long-span bridges in complex terrains. Further improvements may be achieved by establishing realistic boundary conditions by combining, for example, microscale and mesoscale flow simulations.

CRediT authorship contribution statement

Etienne Cheynet: Conceptualization, Methodology, Software, Validation, Formal analysis, Investigation, Resources, Data curation, Writing - original draft, Writing - review & editing, Visualization, Supervision, Project administration. **Shengnan Liu:** Conceptualization, Methodology, Software, Validation, Investigation, Data curation, Writing - review & editing. **Muk Chen Ong:** Resources, Writing - review & editing, Project administration, Funding acquisition. **Jasna Bogunović Jakobsen:** Resources, Writing - review & editing. **Jónas Snæbjörnsson:** Resources, Writing - review & editing. **Inno Gatin:** Conceptualization, Methodology, Software, Writing - review & editing.

Declaration of competing interest

The authors declare that they have no known competing financial interests or personal relationships that could have appeared to influence the work reported in this paper.

References

Arthur, R.S., Lundquist, K.A., Mirocha, J.D., Chow, F.K., 2018. Topographic effects on radiation in the WRF model with the immersed boundary method: implementation, validation, and application to complex terrain. Mon. Weather Rev. 146, 3277–3292.

Astrup, P., Mikkelsen, T., Jensen, N., 1997. A fast model for mean and turbulent wind characteristics over terrain with mixed surface roughness. Radiat. Protect. Dosim. 73, 257–260.

Baik, J.-J., Park, S.-B., Kim, J.-J., 2009. Urban flow and dispersion simulation using a CFD model coupled to a mesoscale model. Journal of Applied Meteorology and Climatology 48, 1667–1681.

Barcons, J., Avila, M., Folch, A., 2018. A wind field downscaling strategy based on domain segmentation and transfer functions. Wind Energy 21, 409–425.

Bilal, M., Birkelund, Y., Homola, M., Virk, M.S., 2016. Wind over complex terrain–microscale modelling with two types of mesoscale winds at Nygårdsfjell. Renew. Energy 99, 647–653.

Blocken, B., 2014. 50 years of computational wind engineering: past, present and future. J. Wind Eng. Ind. Aerod. 129, 69–102.

Blocken, B., van der Hout, A., Dekker, J., Weiler, O., 2015. CFD simulation of wind flow over natural complex terrain: case study with validation by field measurements for Ria de Ferrol, Galicia, Spain. J. Wind Eng. Ind. Aerod. 147, 43–57.

Bowen, A., 2003. Modelling of strong wind flows over complex terrain at small geometric scales. J. Wind Eng. Ind. Aerod. 91, 1859–1871.

Burlando, M., Carassale, L., Georgieva, E., Ratto, C.F., Solari, G., 2007a. A simple and efficient procedure for the numerical simulation of wind fields in complex terrain. Boundary-Layer Meteorol. 125, 417–439.

Burlando, M., Georgieva, E., Ratto, C.F., 2007b. Parameterisation of the planetary boundary layer for diagnostic wind models. Boundary-Layer Meteorol. 125, 389–397.

Cermak, J., 1984. Physical modelling of flow and dispersion over complex terrain. Boundary-Layer Meteorol. 30, 261–292.

Charnock, H., 1955. Wind stress on a water surface. Q. J. R. Meteorol. Soc. 81, 639–640.

Cheynet, E., Jakobsen, J.B., Snæbjörnsson, J., 2016a. Buffeting response of a suspension bridge in complex terrain. Eng. Struct. 128, 474–487.

Cheynet, E., Jakobsen, J.B., Snæbjörnsson, J., Mikkelsen, T., Sjöholm, M., Mann, J., Hansen, P., Angelou, N., Svardal, B., 2016b. Application of short-range dual-Doppler lidars to evaluate the coherence of turbulence. Exp. Fluid 57, 184.

Cheynet, E., Jakobsen, J.B., Snæbjörnsson, J., Angelou, N., Mikkelsen, T., Sjöholm, M., Svardal, B., 2017a. Full-scale observation of the flow downstream of a suspension bridge deck. J. Wind Eng. Ind. Aerod. 171, 261–272.

Cheynet, E., Jakobsen, J.B., Snæbjörnsson, J., Reuder, J., Kumer, V., Svardal, B., 2017b. Assessing the potential of a commercial pulsed lidar for wind characterisation at a bridge site. J. Wind Eng. Ind. Aerod. 161, 17–26.

Cheynet, E., Jakobsen, J., Snæbjörnsson, J., Ágústsson, H., Harstveit, K., 2018. Complementary use of wind lidars and land-based met-masts for wind measurements in a wide fjord. In: Journal of Physics: Conference Series, vol. 1104. IOP Publishing, 012028.

Cheynet, E., Jakobsen, J.B., Snæbjörnsson, J., 2019. Flow distortion recorded by sonic anemometers on a long-span bridge: towards a better modelling of the dynamic wind load in full-scale. J. Sound Vib. 450, 214–230. https://doi.org/10.1016/j.jsv.2019.03.013.

Davenport, A.G., 1961. The application of statistical concepts to the wind loading of structures. Proc. Inst. Civ. Eng. 19, 449–472.

Deaves, D., 1981. Computations of wind flow over changes in surface roughness. J. Wind Eng. Ind. Aerod. 7, 65–94.

Dhunny, A., Lollchund, M., Rughooputh, S., 2017. Wind energy evaluation for a highly complex terrain using computational fluid dynamics (cfd). Renew. Energy 101, 1–9.

Eidsvik, K.J., Holstad, A., Lie, I., Utnes, T., 2004. A prediction system for local wind variations in mountainous terrain. Boundary-Layer Meteorol. 112, 557–586.

EN 1991-1-4, 2005. Eurocode 1: Actions on Structures–Part 1-4: General Actions-Wind Actions.

ESDU, 2001. ESDU 01008, Computer Program for Wind Speeds and Turbulence Properties: Flat or Hilly Sites in Terrain with Roughness Changes.

Farr, T.G., Rosen, P.A., Caro, E., Crippen, R., Duren, R., Hensley, S., Kobrick, M., Paller, M., Rodriguez, E., Roth, L., et al., 2007. The shuttle radar topography mission. Rev. Geophys. 45.

Fenerci, A., 2018. Full-scale investigation of the effects of wind turbulence characteristics on dynamic behavior of long-span cablesupported bridges in complex terrain. Ph.D. thesis NTNU.

Flay, R.G., King, A.B., Revell, M., Carpenter, P., Turner, R., Cenek, P., Pirooz, A.A.S., 2019. Wind speed measurements and predictions over belmont hill, Wellington, New Zealand. J. Wind Eng. Ind. Aerod. 195, 104018.

Fortak, H., 1982. Meteorologie. Reimer.

Grønås, S., Sandvik, A.D., 1999. Numerical simulations of local winds over steep orography in the storm over north Norway on October 12, 1996. J. Geophys. Res.: Atmosphere 104, 9107–9120.

Hacker, J., Draper, C., Madaus, L., 2018. Challenges and opportunities for data assimilation in mountainous environments. Atmosphere 9, 127.

Hargreaves, D., Wright, N.G., 2007. On the use of the k–ε model in commercial CFD software to model the neutral atmospheric boundary layer. J. Wind Eng. Ind. Aerod. 95, 355–369.

Hay, J., 1984. Analyses of wind and response data from the Wye and Erskine bridges and comparison with theory. J. Wind Eng. Ind. Aerod. 17, 31–49.

Holcombe, S., 2011. Stlwrite - write ASCII or Binary STL files. https://www.mathworks.com/matlabcentral/fileexchange/20922-stlwrite-write-ascii-or-binary-stl-files.

Hu, P., Li, Y., Huang, G., Kang, R., Liao, H., 2015. The appropriate shape of the boundary transition section for a mountain-gorge terrain model in a wind tunnel test. Wind Struct. 20, 15–36.

Hu, P., Han, Y., Xu, G., Li, Y., Xue, F., 2018. Numerical simulation of wind fields at the bridge site in mountain-gorge terrain considering an updated curved boundary transition section. J. Aero. Eng. 31, 04018008.

Huang, G., Cheng, X., Peng, L., Li, M., 2018. Aerodynamic shape of transition curve for truncated mountainous terrain model in wind field simulation. J. Wind Eng. Ind. Aerod. 178, 80–90.

Jackson, P.L., Steyn, D.G., 1994. Gap winds in a fjord. Part I: observations and numerical simulation. Mon. Weather Rev. 122, 2645–2665.

Jasak, H., 2009. OpenFOAM: open source CFD in research and industry. International Journal of Naval Architecture and Ocean Engineering 1, 89–94.

Jasak, H., Weller, H., Gosman, A., 1999. High resolution NVD differencing scheme for arbitrarily unstructured meshes. Int. J. Numer. Methods Fluid. 31, 431–449.

Jensen, N., Hjort-Hansen, E., 1977. Dynamic Excitation of Structures by Wind—turbulence and response measurements at the Sotra Bridge, p. 78003. Report No. STF71 A.

Juretić, F., 2017. cfMesh: Advanced Meshing Tool. cfMesh.com. Online; accessed 22 February 2017.

Kalnay, E., Kanamitsu, M., Kistler, R., Collins, W., Deaven, D., Gandin, L., Iredell, M., Saha, S., White, G., Woollen, J., et al., 1996. The NCEP/NCAR 40-year reanalysis project. Bull. Am. Meteorol. Soc. 77, 437–472.

Kervyn, M., Ernst, G., Goossens, R., Jacobs, P., 2008. Mapping volcano topography with remote sensing: ASTER vs. SRTM. Int. J. Rem. Sens. 29, 6515–6538.

Kristensen, L., Jensen, N., 1979. Lateral coherence in isotropic turbulence and in the natural wind. Boundary-Layer Meteorol. 17, 353–373.

Lange, B., Højstrup, J., 2001. Evaluation of the wind-resource estimation program WAsP for offshore applications. J. Wind Eng. Ind. Aerod. 89, 271–291.

Li, Y., Hu, P., Xu, X., Qiu, J., 2017. Wind characteristics at bridge site in a deep-cutting gorge by wind tunnel test. J. Wind Eng. Ind. Aerod. 160, 30–46.

Lun, Y.F., Mochida, A., Murakami, S., Yoshino, H., Shirasawa, T., 2003. Numerical simulation of flow over topographic features by revised k–ε models. J. Wind Eng. Ind. Aerod. 91, 231–245.

Lundquist, K.A., Chow, F.K., Lundquist, J.K., 2010. An immersed boundary method for the weather research and forecasting model. Mon. Weather Rev. 138, 796–817.

Lundquist, K.A., Chow, F.K., Lundquist, J.K., 2012. An immersed boundary method enabling large-eddy simulations of flow over complex terrain in the WRF model. Mon. Weather Rev. 140, 3936–3955.

Lystad, T.M., Fenerci, A., Øiseth, O., 2018. Evaluation of mast measurements and wind tunnel terrain models to describe spatially variable wind field characteristics for long-span bridge design. J. Wind Eng. Ind. Aerod. 179, 558–573.

Mahrer, Y., 1984. An improved numerical approximation of the horizontal gradients in a terrain-following coordinate system. Mon. Weather Rev. 112, 918–922.

Mattuella, J., Loredo-Souza, A., Oliveira, M., Petry, A., 2016. Wind tunnel experimental analysis of a complex terrain micrositing. Renew. Sustain. Energy Rev. 54, 110–119.

McAuliffe, B.R., Larose, G.L., 2012. Reynolds-number and surface-modeling sensitivities for experimental simulation of flow over complex topography. J. Wind Eng. Ind. Aerod. 104, 603–613.

Menke, R., Vasiljević, N., Mann, J., Lundquist, J.K., 2019. Characterization of flow recirculation zones at the Perdigão site using multi-lidar measurements. Atmos. Chem. Phys. 19, 2713–2723.

Meroney, R.N., 1980. Wind-tunnel simulation of the flow over hills and complex terrain. J. Wind Eng. Ind. Aerod. 5, 297–321.

Murakami, S., 1997. Current status and future trends in computational wind engineering. J. Wind Eng. Ind. Aerod. 67, 3–34.

Oltmanns, M., Straneo, F., Moore, G., Mernild, S.H., 2014. Strong downslope wind events in Ammassalik, southeast Greenland. J. Clim. 27, 977–993.

Petersen, E.L., Mortensen, N.G., Landberg, L., Højstrup, J., Frank, H.P., 1998. Wind power meteorology. Part II: siting and models. Wind Energy: An International Journal for Progress and Applications in Wind Power Conversion Technology 1, 55–72.

Powers, J.G., Klemp, J.B., Skamarock, W.C., Davis, C.A., Dudhia, J., Gill, D.O., Coen, J.L., Gochis, D.J., Ahmadov, R., Peckham, S.E., et al., 2017. The weather research and forecasting model: overview, system efforts, and future directions. Bull. Am. Meteorol. Soc. 98, 1717–1737.

Rasheed, A., Sørli, K., 2013. CFD analysis of terrain induced turbulence at Kristiansand airport. Kjevik. *Aviation* 17, 104–112.

Ratto, C., Festa, R., Romeo, C., Frumento, O., Galluzzi, M., 1994. Mass-consistent models for wind fields over complex terrain: the state of the art. Environ. Software 9, 247–268.

Richards, P., Hoxey, R., 1993. Appropriate boundary conditions for computational wind engineering models using the k–ε turbulence model. J. *Wind Eng. Ind. Aerod.* 46, 145–153.

Rodrigues, C.V., Palma, J., Vasiljević, N., Courtney, M., Mann, J., 2016. Coupled simulations and comparison with multi-lidar measurements of the wind flow over a double-ridge. In: Journal of Physics: Conference Series, vol. 753. IOP Publishing, 032025.

Schmidli, J., Böing, S., Fuhrer, O., 2018. Accuracy of simulated diurnal valley winds in the Swiss Alps: influence of grid resolution, topography filtering, and land surface datasets. Atmosphere 9, 196.

Shamarock, W., Klemp, J., Dudhia, J., Gill, D., Barker, M., Wang, W., Powers, J., 2008. A Description of the Advanced Research WRF Version 3: NCAR Technical Note. Technical Report National Center for Atmospheric Research.

Sherman, C.A., 1978. A mass-consistent model for wind fields over complex terrain. J. Appl. Meteorol. 17, 312–319.

Shih, T.-H., Liou, W.W., Shabbir, A., Yang, Z., Zhu, J., 1995. A new k–ε eddy viscosity model for high Reynolds number turbulent flows. Comput. Fluid 24, 227–238.

Solari, G., Piccardo, G., 2001. Probabilistic 3-D turbulence modeling for gust buffeting of structures. Probabilist. Eng. Mech. 16, 73–86.

Song, J.-L., Li, J.-W., Flay, R.G., 2020. Field measurements and wind tunnel investigation of wind characteristics at a bridge site in a Y-shaped valley. J. Wind Eng. Ind. Aerod. 202, 104199.

Steiwer, G.W.H., 2017. Nasjonal detaljert høydemodell-homogenitetsanalyse av terrengmodell fra flybåren laserskanning. Master's thesis NTNU.

Strømmen, E., Hjorth-Hansen, E., 1995. The buffeting wind loading of structural members at an arbitrary attitude in the flow. J. Wind Eng. Ind. Aerod. 56, 267–290.

Tachikawa, T., Kaku, M., Iwasaki, A., Gesch, D., Oimoen, M., Zhang, Z., Danielson, J., Krieger, T., Curtis, B., Haase, J., Michael, A., Carabajal, C., 2011. ASTER Global Digital Elevation Model Version 2–Summary of Validation Results August 31, 2011. Technical Report Earth Resources Observation and Science (EROS) Center.

Tang, X.-Y., Zhao, S., Fan, B., Peinke, J., Stoevesandt, B., 2019. Micro-scale wind resource assessment in complex terrain based on CFD coupled measurement from multiple masts. Appl. Energy 238, 806–815.

Tang, H., Li, Y., Shum, K.M., Xu, X., Tao, Q., 2020. Non-uniform wind characteristics in mountainous areas and effects on flutter performance of a long-span suspension bridge. J. Wind Eng. Ind. Aerod. 201, 104177.

Temel, O., Bricteux, L., van Beeck, J., 2018. Coupled WRF-OpenFOAM study of wind flow over complex terrain. J. Wind Eng. Ind. Aerod. 174, 152–169.

Toja-Silva, F., Kono, T., Peralta, C., Lopez-Garcia, O., Chen, J., 2018. A review of computational fluid dynamics (cfd) simulations of the wind flow around buildings for urban wind energy exploitation. J. Wind Eng. Ind. Aerod. 180, 66–87.

Van Zyl, J.J., 2001. The shuttle radar topography mission (srtm): a breakthrough in remote sensing of topography. Acta Astronaut. 48, 559–565.

Wang, J., Li, L., Jakobsen, J.B., Haver, S.K., 2019. Metocean conditions in a Norwegian fjord in relation to the floating bridge design. J. Offshore Mech. Arctic Eng. 141, 021604.

Wieringa, J., 1993. Representative roughness parameters for homogeneous terrain. Boundary-Layer Meteorol. 63, 323–363.

Zhang, M.H., 2015. Wind resource assessment and micro-siting: science and engineering. John Wiley & Sons.

Zhu, L., Xu, Y., 2005. Buffeting response of long-span cable-supported bridges under skew winds. Part 1: theory. J. Sound Vib. 281, 647–673.

Zhu, L., Xu, Y., Zhang, F., Xiang, H., 2002. Tsing Ma bridge deck under skew winds - Part I: aerodynamic coefficients. J. Wind Eng. Ind. Aerod. 90, 781–805.